Failure analysis of the effects of porosity in thermally oxidised nuclear graphite using finite element modelling

7 authors, including:

Christophe Berre
Institut Universitaire de Technologie de Nîmes
9 PUBLICATIONS   139 CITATIONS

SEE PROFILE

Alex S L Fok
University of Minnesota Twin Cities
250 PUBLICATIONS   3,333 CITATIONS

SEE PROFILE

Paul Mummery
The University of Manchester
175 PUBLICATIONS   2,770 CITATIONS

SEE PROFILE

Barry J. Marsden
The University of Manchester
136 PUBLICATIONS   1,924 CITATIONS

SEE PROFILE

Some of the authors of this publication are also working on these related projects:

Intergranular SCC View project

A technical and environmental appraisal of recycled carbon fibre materials View project

Failure analysis of the effects of porosity in thermally oxidised nuclear graphite using Finite Element modelling[1]

C. Berre[1], S.L. Fok[*1], P.M. Mummery[2], J. Ali[2],

B.J. Marsden[1], T.J. Marrow[2], G. B. Neighbour[3]

[1]*School of Mechanical, Aerospace and Civil Engineering, University of Manchester, PO Box 88, Sackville Street, Manchester, M60 1QD, UK*
[2]*School of Materials, University of Manchester, Grosvenor Street, Manchester, M1 7HS, UK*
[3]*Dept. of Engineering, University of Hull, Cottingham Road, Hull, HU6 7RX, UK*

Abstract

Finite Element models of thermally oxidised nuclear graphite were generated using three-dimensional high-resolution tomography images. Bulk tensile strength was then evaluated using a smeared-crack model, which shows an exponential decay in the bulk strength with increasing pore volume. The Finite Element results were in good agreement with radiolytic oxidation experiments. A stochastic analysis using a modified Weibull theory was also performed to describe the evolution of the failure process with increasing load for different levels of porosities.

1.   Introduction

Graphite is a polycrystalline material with excellent thermal and mechanical properties at high temperatures, which makes it particularly suitable for a large range of industrial applications. In the nuclear industry, graphite is used for the construction of the moderator as well as structural components of the reactor core. During service, however, this material is subjected to neutronic irradiation, and in some cases radiolytic oxidation, resulting in significant changes to its microstructures and properties. The

---

[*] Corresponding Author. Tel.: +44 (0) 161-275-4327; fax: +44-161-275-4328. *E-mail address:* alex.fok@manchester.ac.uk

accurate prediction of these irradiation-induced changes is essential in the design, operation and safety assessment of graphite-moderated reactors. Both analytical and numerical models are being developed to complement materials testing and to provide a mechanistic understanding of the relationships between microstructural and bulk property changes [1].

Novel computer-based and image processing technologies have proved to be very powerful for investigating the microstructures of materials and their relationships with the physical properties. The basic principles of micro-tomography used for such investigations and the effects of thermal oxidation on some of graphite's physical properties analysed using this technique can be found in [1] and [2]. For practical reasons, thermal oxidation in air or CO_2 is often used to simulate the changes due to radiolytic oxidation [3].

In a recent work carried out by the authors [4], detailed 3-dimensional Finite Element (FE) models of a graphite's microstructure were created from X-ray tomography images and used to evaluate bulk mechanical properties such as Young's modulus and strength. The effect of oxidation was mimicked by adjusting the greyscale of the images so as to increase the pore volume artificially. The results seemed to show good agreement with data obtained from radiolytic oxidation.

In the present work, Gilsocarbon graphite samples thermally oxidised to different levels were scanned using X-ray tomography and the resulting images converted into accurate FE models [5]. FE analysis was then performed using commercial software [6] to predict the bulk tensile strength of the material and the results compared with those in the literature. The development of failure in these models was also analysed in detail. The type of graphite considered is that used in the UK Advanced Gas-Cooled Reactors (AGR), which is quasi-isotropic and composed initially of 20% porosity, a coal-tar pitch binder matrix and nearly spherical filler coke particles, both being by-products of the petroleum industry [7].

2. Radiolytic vs. thermal oxidation

In the AGRs, thermal oxidation of the graphite moderator does not occur since the temperature of the surrounding CO_2 gas coolant is below 600^0C, and radiolytic

oxidation is the preponderant phenomenon causing changes in its physical properties. In radiolytic oxidation, which occurs uniformly throughout the graphite specimen [8], carbon dioxide molecules of the coolant gas are activated by ionising radiation [9] and the resulting oxidising species may react with the carbon atoms of the graphite structure on the pore surfaces as described by

$$CO_2 + Radiation \rightarrow CO_2^* + C(gr.) \rightarrow 2\,CO$$ (1)
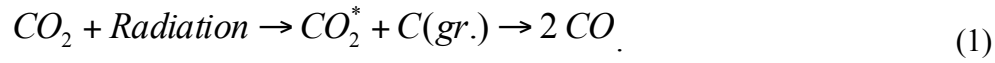
However, since the lifetime of the oxidising species is very short, those produced in close proximity of the pore surfaces are more likely to reach and react with the surface of the material. As a result, pores having a diameter less than 2 μm are more reactive than larger pores.

During thermal oxidation, as in radiolytic oxidation, the carbon atoms in the graphite material react with the carbon dioxide molecules, giving rise to the production of carbon monoxide. But the changes in strength and elastic modulus are more severe in thermal oxidation than in radiolytic oxidation. Due to the greater reactivity of carbon atoms located on the edges of the basal plane than those at mid-span, fine narrow slit-shaped pores develop in the binder phase during thermal oxidation [10].

3. Definition of the Finite Element model

3.1. Image segmentation

Samples of virgin and thermally oxidised Gilsocarbon were scanned using X-ray micro-tomography with a 26 μm resolution (Fig.1).
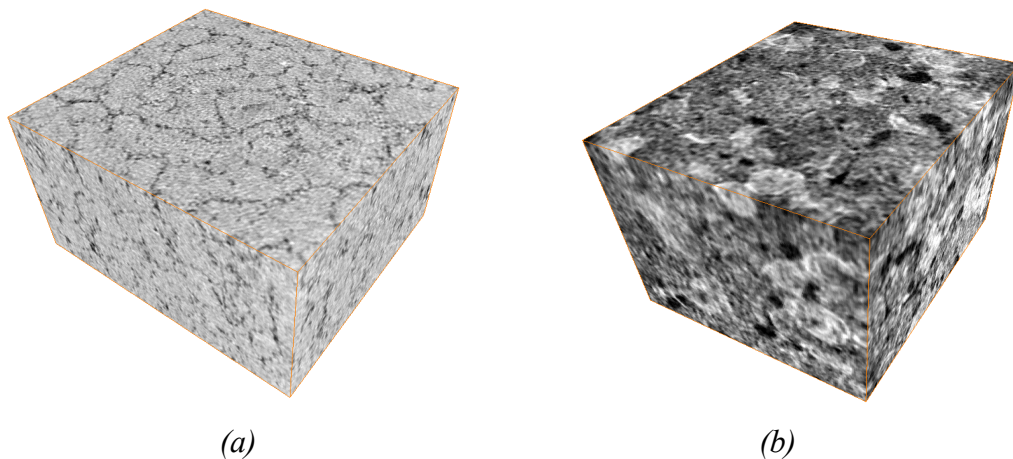

(a)   *(b)*

Fig. 1: Three-dimensional images reconstructed from X-ray tomography of (a) virgin and (b) thermally oxidised Gilsocarbon.

The density of each sample was evaluated by measuring the mass of the sample on a micro-scale, and by calculating the volume of the reconstructed three-dimensional image. Densities ranging from 0.72 to 1.7 g/cm^3 were found. These are related to the pore volume fraction P and the fractional weight loss x by

$$P = \frac{\rho_0}{\rho_c}(x-1)+1 \quad,$$

(2)

where ρ_c is the theoretical crystal density of graphite, i.e. 2.26 g/cm^3, and ρ_0 is the bulk density of virgin graphite. It should be pointed out that numerical models containing over 0.5 cm^3/cm^3 pore volume fraction could not be analysed because of the substantial loss of load path across the samples.

In order to ensure numerical stability when performing the non-linear failure analysis, it was necessary to remove noise and sharp corners from the raw images as these were a source of stress singularities causing numerical instability. This first step of image processing, the so-called image segmentation which is carried out before mesh generation, is often critical as the accuracy and stability of the resulting numerical model depends on this process and un-realistic models may result if it is not conducted properly. The image segmentation step was carried out using the ImageJ software [11]. Firstly, a region of interest was selected from the middle of the raw image and a median filter was applied to minimize the noise by calculating the average greyscale in a voxel from those in the neighbouring voxels. The contours of the image were then "smoothed". To complete the image processing step, a greyscale threshold was manually adjusted to establish the pore/material boundaries and to obtain the required pore volume in the model, according to the density measured. Fig2 shows a three-dimensional mesh resulting from the tomography scan of an oxidised sample.
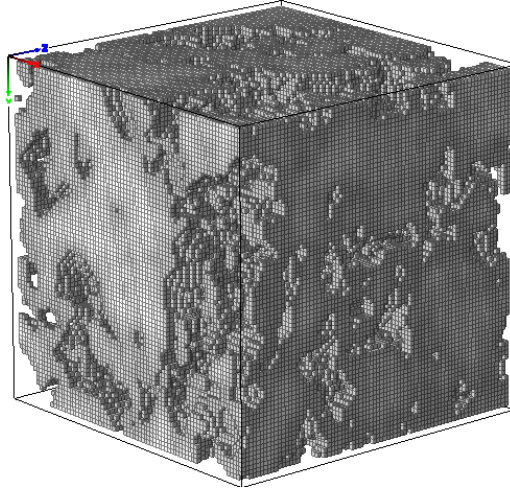
Fig. 2: Three-dimensional Finite Element mesh generated from X-ray tomography scan of thermally oxidised Gilsocarbon.

Finally, to maximise the volume of the model, which was limited by the total number of elements, the resolution of the raw image was decreased to 40 μm (by "down-sampling") using the nearest-neighbour method [5]. In this way, the volume of study could be extended to $V = (1.2\ mm)^3$. The effect of this down-sampling on the numerical solution was investigated by a convergence study (section 3.3). To avoid any element orientation sensitivity during crack formation, the models used eight-noded cubic elements with a reduced-integration scheme (ABAQUS C3D8R [6]). As a first assumption, only porosity and graphite material were segmented in the numerical models, filler particles and binder phase were not separated.

3.2. Definition of the failure model

A smeared-crack approach [12] was used to model material failure in graphite and to evaluate the effects of oxidation on the tensile strength. Damage and cracking, which are evenly distributed within the volume, are modelled by a continuum whose mechanical properties are weakened by overload. Tortuousity of the crack can also be represented by such a method [13]. Disadvantages of the method are possible mesh sensitivity and numerical instability due to the large number of stress concentrations or even stress singularities generated around poorly defined pores. To minimise the numerical instability caused by these high stress concentrations, the Riks method [14, 15] implemented in ABAQUS [6] has proved to be the most efficient solver method

and was used in our analysis. Fig. 3 shows schematically the stress-strain curve used to define the material failure behaviour.
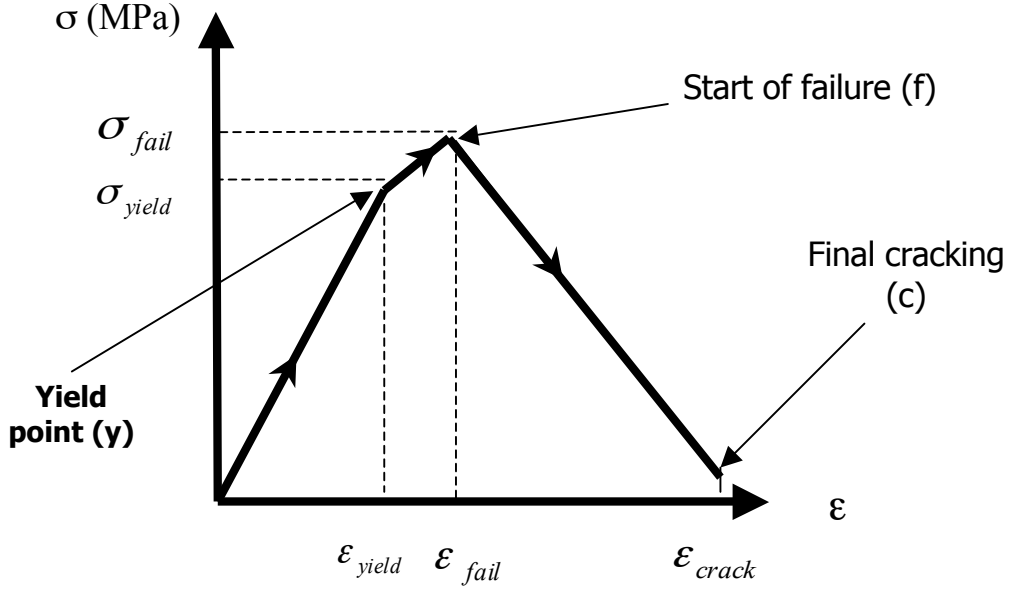

Fig. 3: Schematic of the smeared failure model for graphite.

Referring to Fig. 3, the assumed intrinsic material behaviour is linear elastic during the first part of loading until the yield point (y) is reached. After a very short yield strain, as graphite is a quasi-brittle material, failure (f) in the form of stress reduction with increasing strain begins. Thereafter, as the strain continues to increase, the stress in the material decreases further until final cracking (c) takes place. The bulk tensile strength $\overline{\sigma}_{fail}$ of a graphite sample is defined as the highest stress reached by the derived strain-stress curve of the numerical model during a simulated uniaxial tensile test. It was calculated by

$$\overline{\sigma}_{fail} = \frac{R_f}{S} \tag{3}$$

where R_f is the maximum reaction force obtained at the fixed surface of the Finite Element model and S is the surface area.

To minimise the size of the problems, the number of elements in each of the models was limited to 20,000, which corresponds to a volume of $V = (1.2 \ mm)^3$ with a 40 μm

resolution. To set up the intrinsic failure model, the following local material parameters for pore-free graphite needed to be defined (see Fig. 3): yield and failure stresses (σ_{yield}, σ_{fail}), failure strain (ε_{fail}), and strain at final cracking (ε_{crack}). To do so, the failure of virgin graphite, which has a pore volume of about 20% and whose bulk properties are well established, was first considered. The intrinsic material parameters for pore-free graphite were determined through a trial-and-error process which aimed to reproduce the bulk properties of virgin graphite using a model with 20% pore volume. The bulk properties of virgin graphite used are summarised in table below.

Porosity	Young's modulus	Poisson's ratio	Tensile strength
20 %	10.85 GPa	0.21	17.5 MPa

Table 1: Bulk mechanical properties of Gilsocarbon [16].

The bulk tensile strength depends largely on the input tensile stress σ_{fail}, which represents the strength of "pore-free" graphite. A value of 57 MPa for this parameter was found to be able to produce a bulk tensile strength of 17.5 MPa using the model for virgin graphite, so this was chosen to be the value for $\overline{\sigma}_{fail}$. As virgin graphite is a quasi-brittle material, the small amount of yielding prior to failure was neglected. Thus, the intrinsic tensile strain at failure can be approximated by

$$\varepsilon_{fail} \cong \frac{\overline{\sigma}_{fail}}{E_0} \tag{4}$$

where E_0 is Young's modulus of pore-free graphite, which was estimated using nano-indentation to be $E_0 = 15\ GPa$. In the smeared-crack model, the post-failure behaviour is determined by the difference between the strain at cracking and the strain at the start of failure, i.e. $\varepsilon_{crack} - \varepsilon_{fail}$ (see Fig. 3). This difference in strains is also called the tension stiffening parameter and its value is commonly determined using experiments [6]. The tension stiffening effects were analysed by varying its value in the model of virgin graphite and observing the changes in the stress-strain curve and the bulk tensile strength. Values of tension stiffening between 0.01 and 0.5 were considered. However, values below 0.05 led to a premature stop of the calculation, and no tensile strength

could be obtained in these cases. Fig. 4 below shows the stress-strain curves for different values of $\varepsilon_{crack} - \varepsilon_{fail}$.
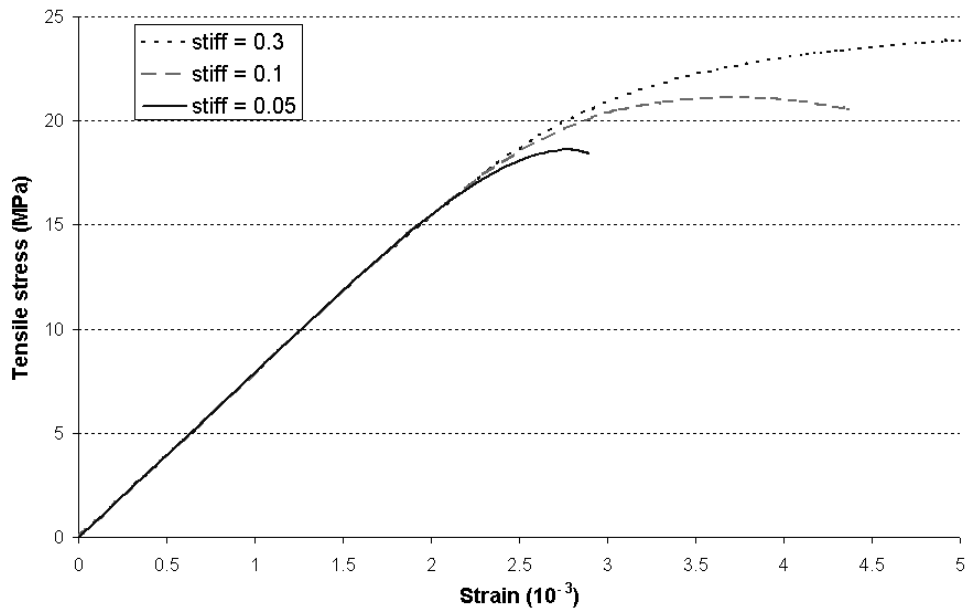

Fig. 4: Effects of tension stiffening ("stiff") on the stress-strain curve of virgin graphite.

It can be seen from Fig. 2 that increasing tension stiffening increases both the maximum stress and the nonlinear behaviour of the model for virgin graphite after the initiation of failure. Since virgin Gilsocarbon graphite exhibits little nonlinear behaviour prior to final fracture under tension, the value of $\varepsilon_{crack} - \varepsilon_{fail}$ retained for subsequent failure analysis was 0.05.

3.3. Convergence

To determine the accuracy of the models, the mesh sensitivity of the results was investigated by changing the number of elements in the mesh. Finite element models, having a volume of $V = (1\,mm)^3$ and containing a porosity ratio of $P = 20\%$ and $P = 42\%$, were chosen for the mesh convergence study. In order to change the number of elements, the resolution was gradually reduced during the image segmentation process from $26\,\mu m$ to $100\,\mu m$.
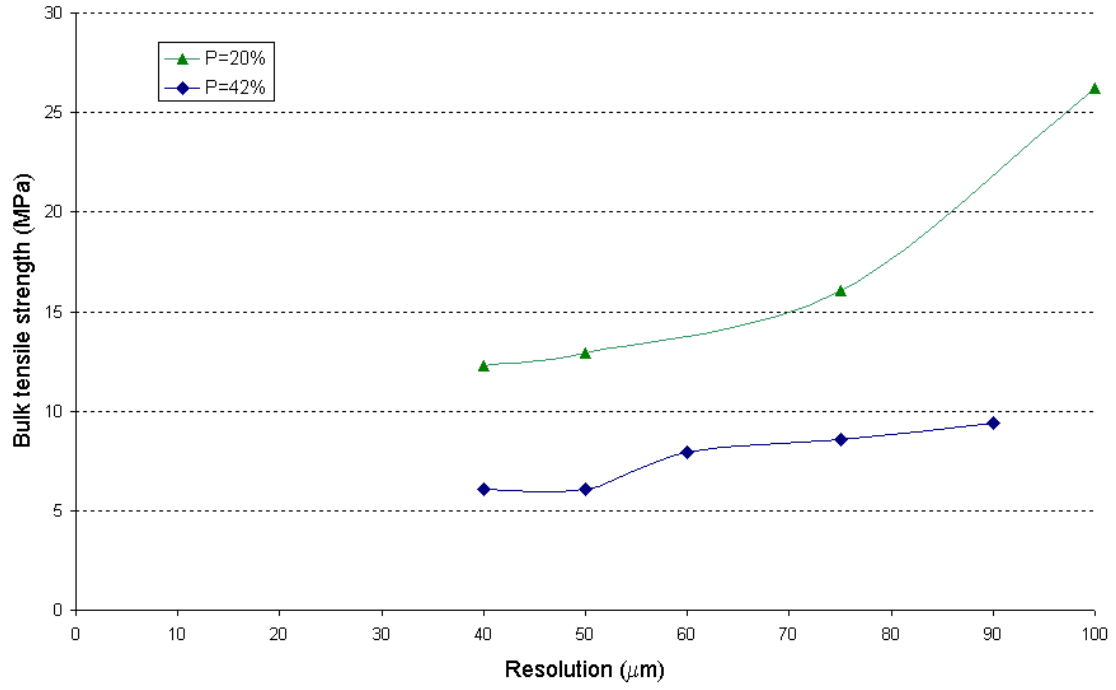
Fig. 5: Convergence of the predicted bulk tensile strengths with increasing resolution.

From Fig. 5, it can be seen that a mesh constructed from images with a 40 *μm* resolution gives reasonably converged solutions for the tensile strength. Higher-resolution models will produce very large amount of files and are not recommended. There is also the problem of increased numerical instability associated with increased mesh density. Increasing the number of elements in the model also increases the likeliness to obtain numerical unstabilities and early stop of the calculation.

4. Results and discussion

4.1. Stress-strain curve analysis

Stresses and strains calculated in the finite element models can be visualised and further analysed using ABAQUS/Viewer [6]. Fig. 6 shows the regions, within two models having different pore volume fractions, in which the axial strain is above the critical failure strain, i.e. $\varepsilon_{fail} = 1.6 \times 10^{-3}$. The displacement load was applied in the direction denoted "3" and the models are viewed throughout the volume (Fig. 6).

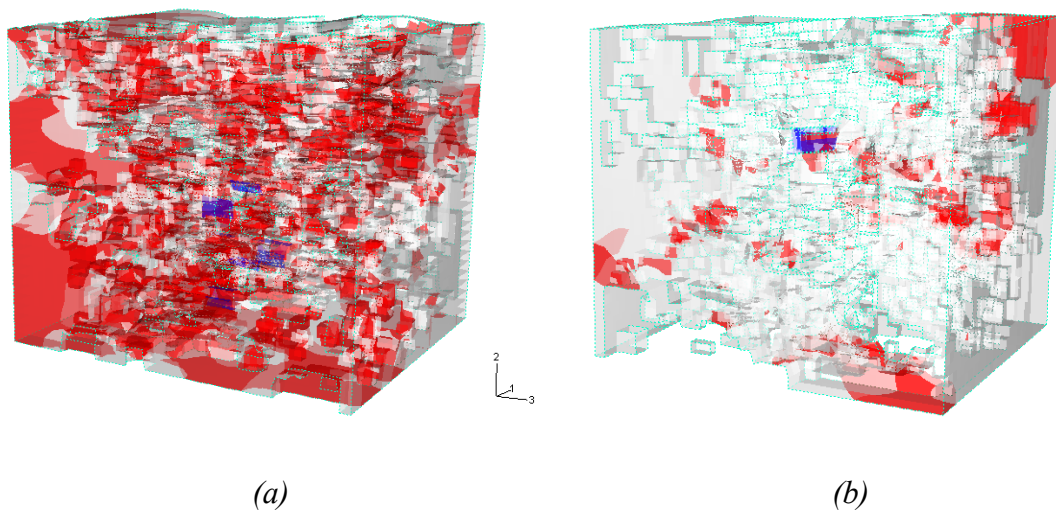*(a)*   *(b)*

Fig. 6: High-strain regions in models containing (a) 21% and (b) 44% porosity before final cracking.

In Fig. 6, the high-strain regions are shown by the darker elements within the volume. It can be noticed that these high-strain regions are more widespread in less porous models, as loading is shared more evenly within them. On the other hand, since high stress concentrations are more localised in small areas within very porous models, numerical instability indicating the onset of failure is more likely to occur sooner in these models. In all the models, material failures initiate in the vicinity of the stress-concentrating pores, coalesce as loading increases and propagate towards the next closest pore or edge. Fig. 7 shows the bulk stress-strain curves obtained with increasing porosity. The ends of the curves indicate termination of the computations due to the onset of numerical instability or unstable crack propagation.
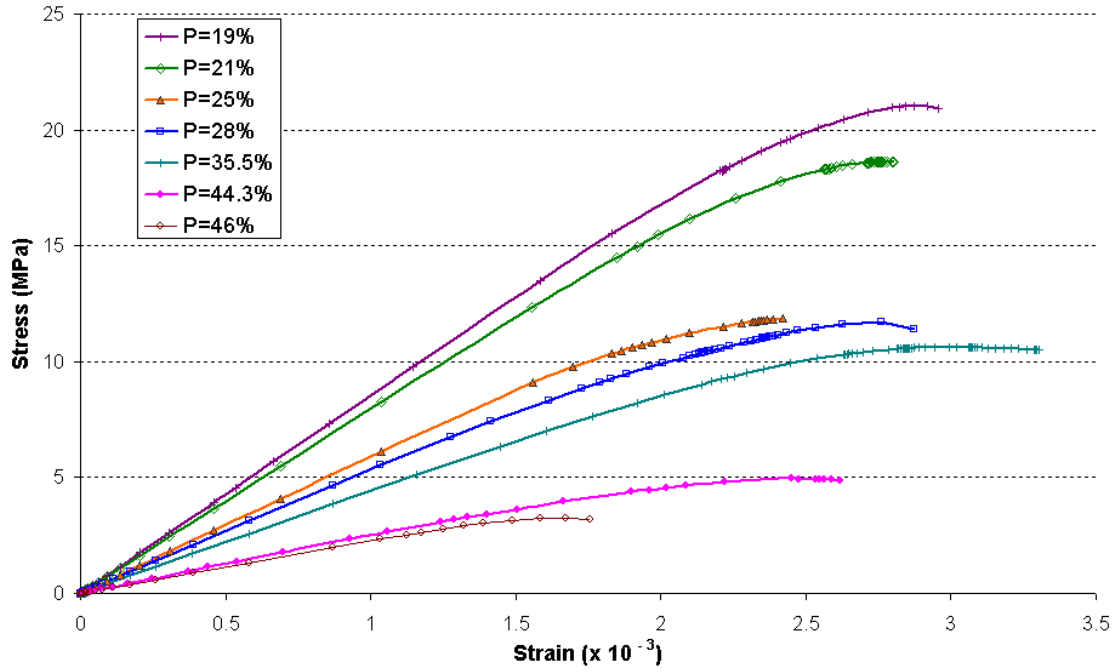
Fig. 7: Stress strain curves of thermally oxidised graphite having different pore volume fractions (P).

In Fig. 7, the peak stress value in the stress-strain curve was taken to be the failure stress of the material. The bulk tensile strength decreases with increasing porosity, and failure occurs at a lower strain value when porosity increases, but compared with the failure stresses the reduction in failure strain is less. The bulk Young's modulus also becomes lower with increasing porosity as expected. However, due to the small sample dimensions and possible significant differences in microstructural arrangements, there are some outliers associated with the highly porous models.

4.2. Bulk tensile strength changes with pore volume fraction

Knowledge of changes in the tensile strength with increasing oxidation or pore volume is important for assessing the integrity of components subjected to oxidation over its service lifetime. The Duckworth-Ryshkewitch relationship [17, 18] is often used to relate the strength σ and the pore volume fraction P in ceramics or brittle materials and is written as

$$\sigma = \sigma_0 \exp(-bP)$$ (5)

where σ_0 is the tensile strength for zero pore volume. In the following study, the pore-free tensile strength determined previously in Section 3.3 was chosen for reference.

In Equation (5), the parameter b determines the rate of decrease in strength with increasing porosities and its value is commonly determined by experiments. It depends on the material, on the property considered and also on the pore shapes [19], which in turn depends on the oxidation process. There seems to be a lack of experimental data on the effect of thermal oxidation on the mechanical properties of graphite. For radiolytic oxidation of Gilsocarbon, Kelly et al. [20] determined experimentally that $b = 4.0$ if Equation (5) is expressed in terms of fractional weight loss x. In terms of pore volume, by equation (2), the value of b for radiolytically oxidised graphite becomes 5.0. The tensile strength at zero porosity is obtained by extrapolating the experimental data to $P = 0$, which gives $\sigma_0 = 47.57\ MPa$. The radiolytic oxidation effect on the bulk tensile strength of such a graphite can therefore be expressed in terms of the pore volume fraction P by

$$\sigma = 47.57\ e^{-5.0\,P}\ .$$

(6)

The bulk tensile strength of thermally oxidised graphite as predicted by the Finite Element models is plotted against the pore volume fraction (P) and compared to (6) in Fig. 8.
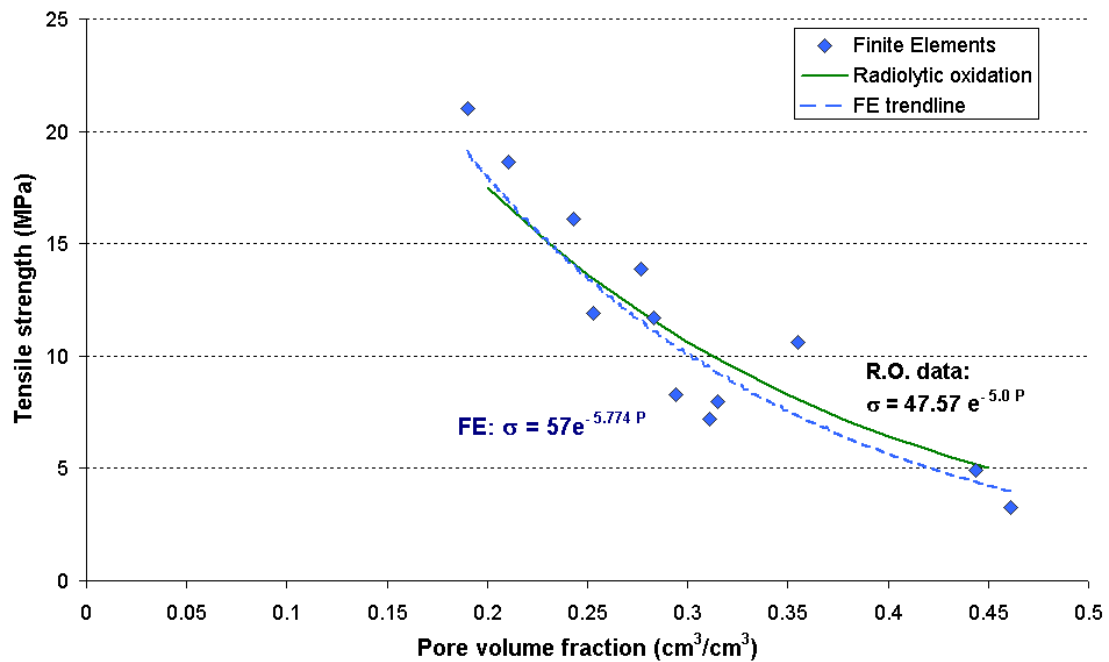

Fig. 8: Predicted bulk tensile strength with increasing pore volume fractions due to thermal oxidation and comparison with radiolytic experiments.

Using the Duckworth-Ryshkewitch relationship, the tensile strength of thermally oxidised Gilsocarbon obtained by Finite Element modelling can be expressed in terms of pore volume fraction (P) by

$$\sigma = 57\, e^{-5.77\,P}\,.$$
(7)

The predicted decay coefficient, $b = 5.77$, is slightly higher than that deduced from radiolytic oxidation data ($b = 5.0$). However, the radiolytic oxidation data seem to fit the numerical results from thermally oxidised samples. This observation is due to the lower value of the tensile strength at zero porosity obtained by extrapolating the experimental radiolytic data ($\sigma_0 = 47.57\,MPa$), compared to the value estimated using a finite element model ($\sigma_0 = 57\,MPa$). If these two values were equal, the decrease of the bulk tensile strength observed in Fig. 8 would be more important in thermal oxidation than in radiolytic oxidation.

4.3. Statistical analysis of failure development

Weibull's stochastic theory [21] is modified to describe the development of failure in the models subjected to a uniaxial displacement, i.e.

$$P_f = 1 - \exp\left[-\left(\frac{\delta}{\delta_0}\right)^m\right]$$
(8)

where P_f is the fraction of elements which has failed when the displacement $u = \delta$, δ_0 is the ultimate displacement, and m is the Weibull modulus.

The Weibull modulus is normally used to give an indication of the scatter in the experimental results, with less scatter being obtained for materials having a higher Weibull modulus. Engineering ceramics commonly have a Weibull modulus around 10 [22], which depends on the manufacturing process as well as the material's microstructure. In this study, the Weibull modulus is used as a measure of the "inhomogeneity" of failure development in the volume of material. The elements in a perfect, homogeneous, defect-free model would all fail at the same time, and therefore the Weibull modulus will be $m = \infty$. "Inhomogeneous" materials, e.g. graphite with high porosity, will have a lower Weibull modulus.

In the numerical analysis, the proportion of elements which has failed can be determined at all stages of loading: from the first element failure to final gross failure. The evolution of failure within the models can be visualised by displaying the strains above the critical strain, i.e. 1.6×10^{-3} (Fig. 9).
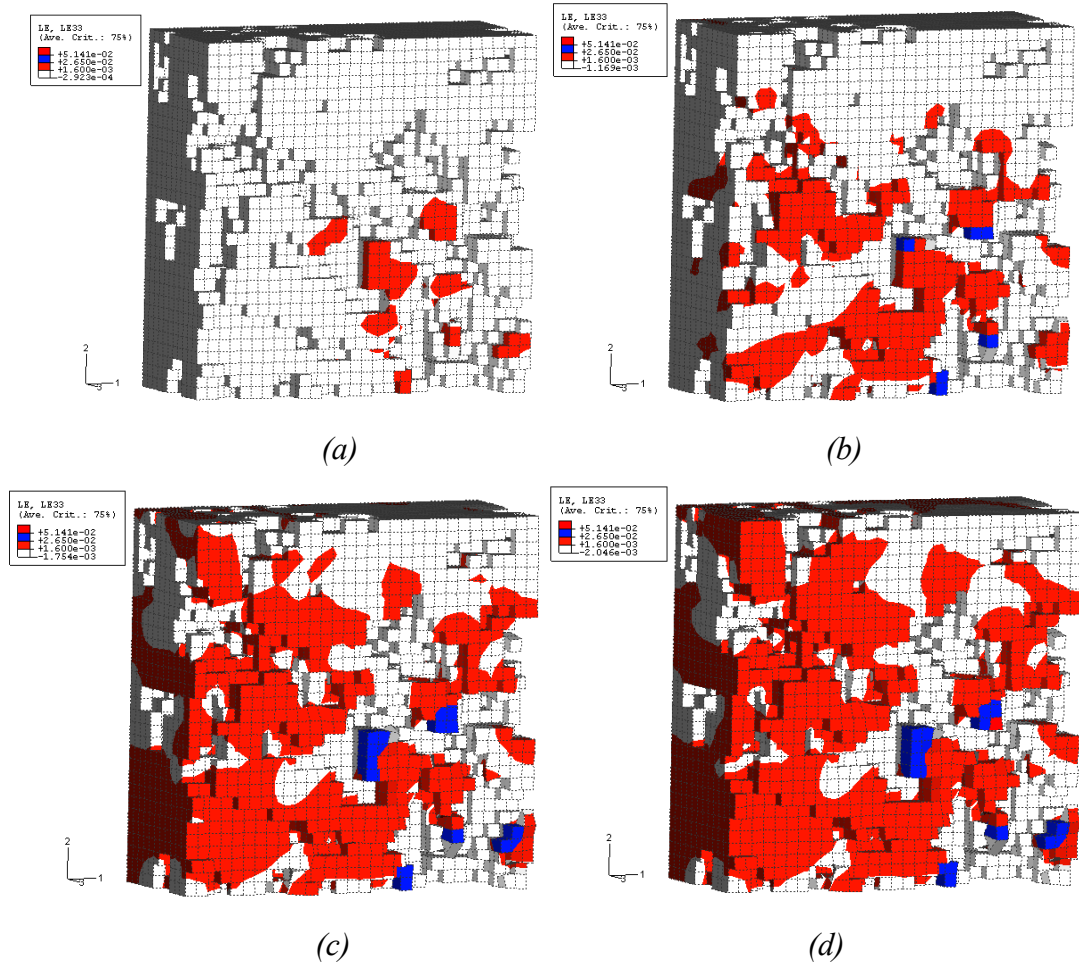

Fig. 9: Evolution of failure in a slice cut-out of a 21% porosity model.

In Fig. 9, failure initiates nearby the pores for a loading corresponding to 40% of final cracking (a), then spreads out for 60% of final cracking (b). At 80% of final cracking (c), failure coalesces until final cracking (d).

Fig. 10 shows the increase in the proportion of failed elements in the numerical models containing different pore volume fractions.
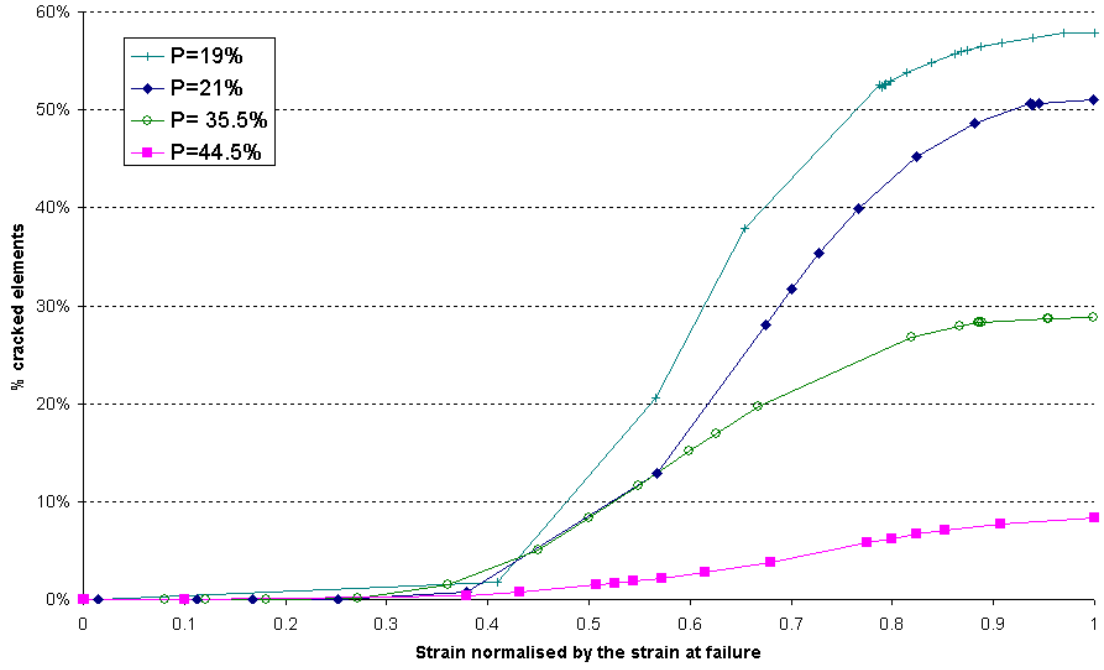
Fig. 10: Evolution of the proportion of cracked elements with increasing load.

It can be seen from Fig. 10 that the number of failed elements at final failure is lower for samples having a higher pore volume fraction. It can also be seen from Fig. 10 that, due to higher stress concentrations around the pores, failure occurs much earlier in models with higher porosities, but the failure development is more gradual than that in a denser material.

In this study, the Weibull modulus indicates how fast failure develops and leads to final cracking. For each numerical model, its value can be determined from equation (9), using the proportion of failed elements F at various stages of loading (δ), i.e.

$$m = \frac{Ln\left[Ln\dfrac{1}{1-P_f}\right]}{Ln\,\delta_0}. \tag{10}$$

The Weibull modulus is determined from the slope of the graph resulting from (10). Finally, m is plotted against the pore volume fraction in Fig. 11.
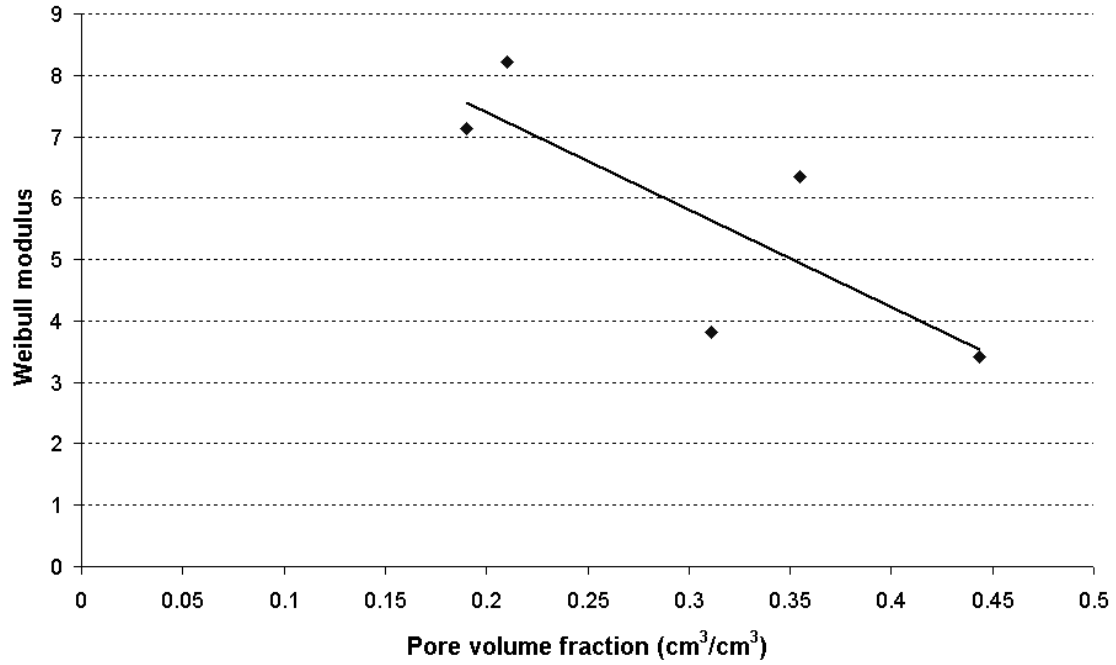
Fig. 11: Evolution of the Weibull modulus with increasing pore volume fractions.

As can be seen from Fig. 11, the Weibull modulus decreases monotonously with increasing porosities. Since the tensile strength is dependent on the microstructural arrangement, this result suggests that high levels of oxidation may induce more scattering in the results, either measured by experiments or calculated by numerical methods.

5. Conclusion

A failure analysis using three-dimensional Finite Element models generated from X-ray tomography images of thermally oxidised Gilsocabon samples was conducted. A smeared-crack failure model originally developed for concrete materials was adopted and numerical predictions were compared with experimental results from the literature. The theoretical "pore-free" tensile strength of Gilsocarbon was evaluated to be $\sigma_0 = 57\ MPa$. Stress-strain curves of graphite under uniaxial tension were produced for different levels of thermal oxidation. Changes in the bulk tensile strength with increasing porosities resulting from thermal oxidation were evaluated and the numerical results were in good agreement with radiolytic oxidation experiments. Finally, a probabilistic analysis of failure development was conducted using a modified Weibull's

theory and the Weibull modulus was found to decrease with increasing porosities, i.e. increasing thermal oxidation.

The apparent agreement between the numerical predictions for thermally oxidised graphite and the experimental data from radiolytic oxidation is perhaps surprising, since, as noticed earlier, thermal oxidation is expected to have a bigger effect on the mechanical properties [1]. Pickup et al. [10] highlighted that fine narrow slit-shaped pores developing in the binder phase were due to the greater reactivity of the edges of the crystallites than the region at mid-span, which implies that the pore tips are in the same scale as the crystallites, i.e. nano-scale. These nano pores greatly affect the microstructural behaviour of the graphite. However, the resolution of X-ray tomography images is generally limited to $\sim 10 \ \mu m$. Therefore, stress concentrations at the pore tips may not be well represented by the numerical models, resulting in the seemingly good agreement with radiolytic and thermal oxidation.

Acknowledgements

Reference

[1] L. Babout, P.M. Mummery, T.J. Marrow, A. Tzelepi, P.J. Withers, The effect of thermal oxidation on polycrystalline graphite studied by X-ray tomography, Carbon 43 (2005) 765—774.

[2] A. C. Kak, M. Slaney M., Principles of Computerized Tomographic Imaging, IEEE Press, 1988.

[3] T.D. Burchell, I.M. Pickup, B. McEnaney, R.G. Cooke, The relationship between microstructure and the reduction of elastic modulus in thermally and radiolytically corroded nuclear graphites, Carbon, 24 (1986) 545—549.

[4] C. Berre, S.L. Fok, B.J. Marsden, L. Babout, A. Hodgkins, T.J. Marrow, P.M. Mummery, Numerical modelling of the effects of porosity changes on the mechanical properties of nuclear graphite, J. Nucl. Mat., 352 (2006) 1—5.

[5] Simpleware Ltd., Scan^{FE} and Scan^{IP} Reference guide Version 2.0, 2005. www.simpleware.co.uk.

[6] HKS, Abaqus reference manual, version 6.4, 2003.

[7] R.E. Nightingale, Nuclear Graphite, Academic Press, London and New-York, 1962.

[8] J.E. Brocklehurst, R.G. Brown, K.E. Gilchrist, V.Y. Labaton, The effect of radiolytic oxidation on the physical properties of graphite, J. Nucl. Mat. 35 (1970) 183—194.

[9] J.V. Best, W.J. Stephen, A.J. Wickham, Radiolytic graphite oxidation, Progr. in Nucl. En. 16 (1985) 127—178.

[10] I.M. Pickup, B. McEnaney, R.G. Cooke, Fracture processes in graphite and effects of oxidation, Carbon 24 (1986) 535—543.

[11] W.S. Rasband, ImageJ, U. S. National Institutes of Health, Bethesda, Maryland, USA, http://rsb.info.nih.gov/ij/, 1997—2005.

[12] Y.R. Rashid, Ultimate strength analysis of prestressed concrete pressure vessels, Nucl. Eng. Design 7 (1968) 334—344

[13] S.P. Shah., S.E. Swartz., C. Ouyang, Fracture mechanics of concrete: applications of fracture mechanics to concrete, rock and other quasi-brittle materials, Wiley Interscience, New-York, 1995.

[14] E. Riks, Application of Newton's method to the problem of elastic stability, J. Appl. Mech. Trans. ASME 39 Ser. E (1972) 1060—1065.

[15] E. Riks, An incremental approach to the solution of snapping and buckling problems, Int. J. Struc. 15 (1979) 529—551.

[16] J.E. Brocklehurst, B.T. Kelly, Analysis of the dimensional changes and structural changes in polycrystalline graphite under fast neutron irradiation, Carbon 31 (1993) 155—178.

[17] W. Duckworth, Discussion of Ryshkewitch paper, J. Am. Ceram. Soc. 36 (1953) 68

[18] Ryshkewitch E., Compression strength of porous sintered alumina and zirconia, 9th communication to ceramography, J. Am. Ceram. Soc. 36 (1953) 65—68.

[19] J. D. Buch, A theoretical derivation of the Knudsen relationship, in Extended Abstracts, 16th Carbon Conference, San Diego, Am. Carb. Soc. (1983) 400—401.

[20] B.T. Kelly, P.A.V. Johnson, P. Schofield, J.E. Brocklehurst, M. Birch, UKAEA northern division studies of the radiolytic oxidation of graphite in carbon dioxide, Carbon 21 (1983) 441—449.

[21] W. Weibull, A statistical distribution function of wide applicability, J. Appl. Mech. 18 (1951) 293–297.

[22] R.W. Rice, Porosity in ceramics, Marcel Dekker, New-York, 1998.